Materials Horizons

Material Descriptors for Thermoelectric Performance of Narrow-gap Semiconductors and Semimetals

Journal:	*Materials Horizons*
Manuscript ID	MH-COM-07-2023-001013.R1
Article Type:	Communication
Date Submitted by the Author:	03-Aug-2023
Complete List of Authors:	Toriyama, Michael; Northwestern University Carranco, Adam; Colorado School of Mines Snyder, G.; Northwestern University Gorai, Prashun; Colorado School of Mines

SCHOLARONE™
Manuscripts

New Concepts

There is a strong need for low-temperature thermoelectric (TE) materials for Peltier cooling and for powering IoT devices. Computational approaches to search and discover new low-temperature TE materials have been limited by material descriptors that do not account for bipolar conduction effects – important in narrow-gap semiconductors and semimetals commonly used for this purpose. In this work, we derive fundamental materials descriptors from Boltzmann transport theory applied to a two-band model, where bipolar conduction effects are considered. We demonstrate the efficacy of these descriptors by re-discovering well-known low-temperature TE materials as well as proposing three new Zintl phases as candidates for future investigation. The proposed descriptors will enable large-scale searches of narrow-gap semiconductors and semimetals for low-temperature TE applications.

Journal Name

ARTICLE TYPE

Cite this: DOI: 10.1039/xxxxxxxxxx

Material Descriptors for Thermoelectric Performance of Narrow-gap Semiconductors and Semimetals †

Michael Y. Toriyama,[a*] Adam N. Carranco,[b] G. Jeffrey Snyder,[a] and Prashun Gorai[b*]

Received Date
Accepted Date

DOI: 10.1039/xxxxxxxxxx

www.rsc.org/journalname

Thermoelectric (TE) cooling is an environment-friendly alternative to vapor compression cooling. New TE materials with high coefficients of performance are needed to further advance this technology. Narrow-gap semiconductors and semimetals have garnered interest for Peltier cooling, yet large-scale computational searches often rely on material descriptors that do not account for bipolar conduction effects. In this work, we derive three material descriptors to assess the TE performances of narrow-gap semiconductors and semimetals – band gap, n- and p-type TE quality factors, and the asymmetry in transport between the majority and minority carriers. We show that a large asymmetry is critical to achieving high TE performance through minimization of bipolar conduction effects. We validate the predictive power of the descriptors by correctly identifying Mg_3Bi_2 and Bi_2Te_3 as high-performing room-temperature TE materials. By applying these descriptors to a broad set of 650 Zintl phases, we identify three candidate room-temperature TE materials, namely $SrSb_2$, Zn_3As_2, and NaCdSb. The proposed material descriptors will enable fast, targeted searches of narrow-gap semiconductors and semimetals for low-temperature TEs. We further propose a refined TE quality factor, B_{bp}, which is a composite descriptor of the peak zT in materials exhibiting significant bipolar conduction; B_{bp} can be used to compare the TE performances of narrow-gap semiconductors.

1 Introduction

The rising demand for cooling, including refrigeration and air conditioning, poses environmental and economic challenges. Conventional cooling systems used in homes, vehicles, industries, and data centers are based on vapor-compression cycles utilizing coolants that are a major source of greenhouse gas emissions.[1–4] The International Energy Agency reported that air conditioning is responsible for almost 20% of the electricity use in buildings globally,[5] with some studies estimating up to 30%–40% usage.[6] Distributed thermoelectric (TE) cooling offers a viable solution,[7] with studies demonstrating TE-based air conditioning[8] and cooling powered by solar energy.[9,10] In addition, low-temperature TE materials have applications in powering Internet of Things (IoT) devices,[11] including low-power Arctic data sensors.[12] Due to their diverse applications, there is a critical need for the discovery and development of low-temperature TE materials.

Historically, narrow-gap semiconductors and semimetals have been found to exhibit good low-temperature TE performance. Bi_2Te_3, with a band gap of 0.14 eV, is the state-of-the-art TE material in the near-room temperature range (300-350 K).[13] The recent demonstration of semimetallic Mg_3Bi_2-based materials with a peak zT of 0.9 at 350 K[14] has renewed interest in low-temperature TE applications.[15–17] Other narrow-gap semiconductors and semimetals such as $CsBi_4Te_6$,[18] $Bi_{1-x}Sb_x$[19], Cd_3As_2,[20] $ZrTe_5$,[21] and correlated materials[22] have also been studied for TE applications at or below room temperature. However, the coefficient of performance of current TE cooling devices ($10\% - 20\%$ of the Carnot limit) is poor compared to vapor compression technology (50% of the Carnot limit under ideal conditions).[7] Since the coefficient of performance increases with the TE figure of merit zT, it is important to search for new TE materials with high zT.

Computations have been instrumental in the discovery and development of new TE materials.[23–28] Large-scale computationally-driven discovery of TE materials requires robust and tractable performance metrics or descriptors. Several such descriptors, including the electronic fitness function,[29,30] Fermi surface complexity factor,[31] and the quality factor[32,33] have been proposed. In developing these material descriptors, it is typically assumed that the charge transport can be ascribed to a single carrier type (electrons or holes) and, therefore, the TE performance can be described within a single parabolic band approximation.[34,35] While this is a reasonable approximation for materials with band gaps that are wide enough to avoid significant bipolar conduction, or even "gapped metals" where a single charge carrier type dominates

[a] Northwestern University, Evanston, IL 60208. [b] Colorado School of Mines, Golden, CO 80401.
* E-mail: michaeltoriyama2024@u.northwestern.edu, pgorai@mines.edu
† Electronic supplementary information available.

This journal is © The Royal Society of Chemistry [year]

transport,[36] it breaks down in materials where both electrons and holes are present in high concentrations, such as narrow-gap semiconductors and semimetals.[37–39] Bipolar conduction increases the electrical conductivity while simultaneously decreasing the Seebeck coefficient and increasing the electronic thermal conductivity.[40] As such, material descriptors for predicting the TE performance of narrow-gap semiconductors and semimetals must account for effects arising from bipolar conduction. One of the co-authors of this study has developed models to estimate the quality factor B – a material descriptor for predicting TE performance.[32] Several high-throughput computational searches for new TE materials have been performed using B as a material descriptor.[33,41–44] However, the models assume charge transport is dominated by either electrons or holes, not both. In this study, we derive new material descriptors for TE performance that account for bipolar conduction effects on charge transport properties.

Using semi-classical Boltzmann transport theory, we derive three important material descriptors for TE performance: (1) band gap, (2) n- and p-type TE quality factors, and (3) asymmetry parameter (ratio of the quality factors). We apply these material descriptors to search for new room-temperature TE materials among narrow-gap and semimetallic Zintl phases. In addition to the Zintl phases, we also calculate the material descriptors for Mg_3Bi_2, Bi_2Te_3, and Bi_2Se_3 as benchmark materials in this study. Consistent with experiments, we show that Mg_3Bi_2 and Bi_2Te_3 are high-performing TE materials near room temperature, which validates the predictive power of the descriptors. Through this search, we identify three Zintl phases ($SrSb_2$, Zn_3As_2, and NaCdSb) with promising room-temperature TE performance. Lastly, we propose a refined TE quality factor, B_{bp}, which is a composite descriptor of the peak zT that can be used to compare the TE performances of narrow-gap semiconductors with significant bipolar conduction effects.

2 Theory: Models and Material Descriptors

Carrier transport is often described in the Boltzmann transport theory framework.[45–47] In the relaxation time approximation, the transport coefficients for isotropic bands is expressed in terms of the transport function $\Sigma(E)$ as,

$$\Sigma(E) = \frac{e^2}{3} \sum_n \tau_n(E) v_n(E)^2 g_n(E) \tag{1}$$

where the summation runs over bands with indices n, $\tau(E)$ is the scattering time, $v(E)$ is the group velocity, and $g(E)$ is the density of states. The 1/3 factor in $\Sigma(E)$ arises from averaging over the three Cartesian directions. The scattering time τ can be expressed as a power law in E for standard scattering mechanisms:

$$\tau(E) \equiv \tau_0 \left(\frac{E}{k_B T}\right)^r \tag{2}$$

where r is a parameter representing the charge scattering mechanism. For example, $r = -1/2$ represents acoustic deformation potential scattering, whereas $r = 1/2$ represents polar optical phonon scattering.[47] There is a growing body of work suggesting polar optical scattering is the dominant scattering mechanism in many polar materials,[48] including PbTe[49–51] and SnSe.[52] As such, we present results for polar optical scattering ($r = 1/2$) in the main text. We provide the analogous results for acoustic deformation potential scattering in the SI and show that the qualitative trends are similar regardless of the scattering mechanism. The transport coefficients, namely the electrical conductivity σ, Seebeck coefficient S, Lorenz number L, and electronic thermal conductivity κ_e, are given by

$$\begin{aligned}
\sigma &= \int \Sigma(E) \left(-\frac{\partial f}{\partial E}\right) dE \\
S &= \frac{k_B}{e} \frac{1}{\sigma} \int \Sigma(E) \left(\frac{E - E_\mathrm{F}}{k_B T}\right) \left(-\frac{\partial f}{\partial E}\right) dE \\
L &= \left(\frac{k_B}{e}\right)^2 \frac{1}{\sigma} \int \Sigma(E) \left(\frac{E - E_\mathrm{F}}{k_B T}\right)^2 \left(-\frac{\partial f}{\partial E}\right) dE - S^2 \\
\kappa_e &= L \sigma T
\end{aligned} \tag{3}$$

where T is the temperature. In cases where carrier transport is dominated by majority carriers and can be described by a single parabolic band, using the power law form of $\tau(E)$ in Eq. (2), the transport coefficients are expressed as,

$$\begin{aligned}
\sigma(\eta) &= \frac{8\pi e}{3} \left(\frac{2 m_e k_B T}{h^2}\right)^{3/2} \mu_w \left(r + \frac{3}{2}\right) F_{r+\frac{1}{2}}(\eta) \\
S(\eta) &= \frac{k_B}{e} \left[-\eta + \frac{r + \frac{5}{2}}{r + \frac{3}{2}} \frac{F_{r+\frac{3}{2}}(\eta)}{F_{r+\frac{1}{2}}(\eta)}\right] \\
L(\eta) &= \left(\frac{k_B}{e}\right)^2 \left[\frac{r + \frac{7}{2}}{r + \frac{3}{2}} \frac{F_{r+\frac{5}{2}}(\eta)}{F_{r+\frac{1}{2}}(\eta)} - \left(\frac{r + \frac{5}{2}}{r + \frac{3}{2}} \frac{F_{r+\frac{3}{2}}(\eta)}{F_{r+\frac{1}{2}}(\eta)}\right)^2\right]
\end{aligned} \tag{4}$$

Here, F_i is the Fermi-Dirac integral, given by

$$F_i(\eta) = \int \frac{\varepsilon^i}{1 + \exp(\varepsilon - \eta)} d\varepsilon \tag{5}$$

where $\eta \equiv E_\mathrm{F}/k_B T$ is the reduced Fermi energy and $\varepsilon \equiv E/k_B T$ is the reduced energy. μ_w is the weighted mobility,[53]

$$\mu_w = \mu_0 \left(\frac{m^*_\mathrm{DOS}}{m_e}\right)^{3/2} = \frac{e\tau_0}{m^*_b} N_V \left(\frac{m^*_b}{m_e}\right)^{3/2} \tag{6}$$

where μ_0 is the intrinsic carrier mobility and m^*_DOS is the density-of-states effective mass, which can be expressed in terms of band effective mass m^*_b and valley degeneracy N_V. The transport coefficients in Eq. (4) must be revised when accounting for the effects of both electrons and holes (two-band model) on TE transport. The theory of the two-band model has been presented in detail elsewhere,[37,54–57] but we briefly review it here to illustrate how the material descriptors are derived.

Here, we adopt the "majority" and "minority" carrier labels so that the theoretical expressions are applicable to both n-type (excess electrons) and p-type (excess holes) materials.[58] We demonstrate that TE transport in narrow-gap semiconductors and semimetals depends on the asymmetry of the majority and minority carrier transport properties. We show this by considering

This journal is © The Royal Society of Chemistry [year]

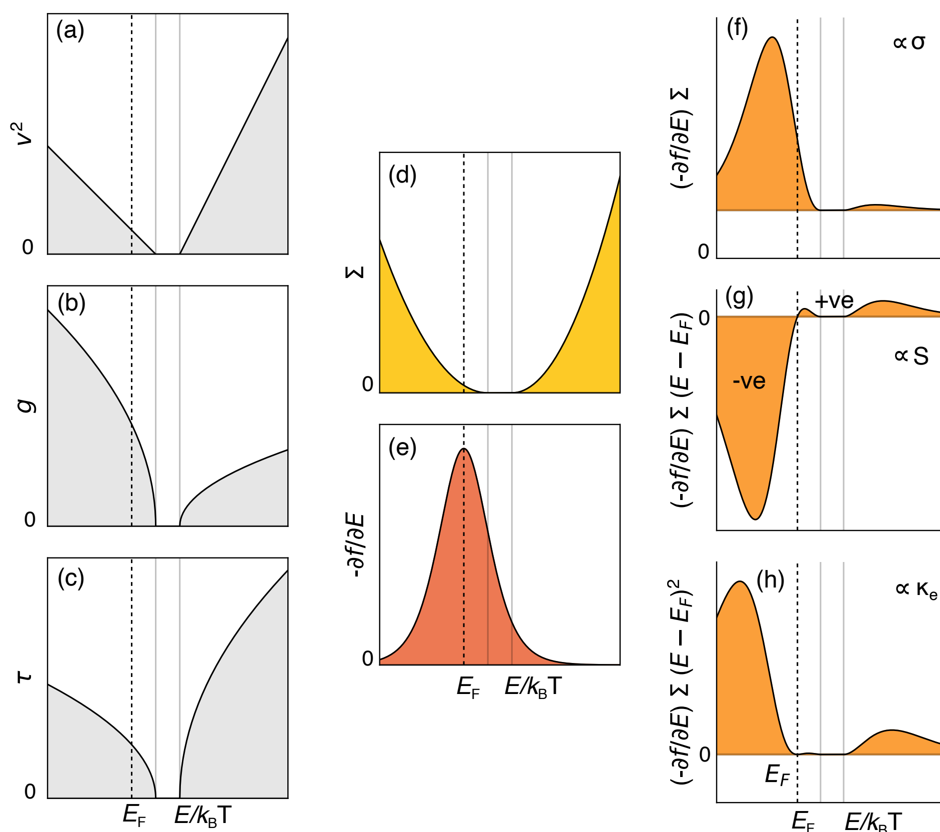

Fig. 1 Transport coefficients in a two-band model. The valence and conduction band edges are shown as solid vertical lines, and the Fermi level E_{F} is shown as a dotted vertical line. (a-c) The components of the transport function $\Sigma(E) = v^2(E)g(E)\tau(E)$, shown in (d), where $v(E)$, $g(E)$, and $\tau(E)$ are the energy-dependent velocity, density of states, and scattering time, respectively. $\Sigma(E)$ is sampled by the selection function $-\partial f/\partial E$, shown in (e), and weighted by $(E - E_{\mathrm{F}})^m$ to obtain (f) the electrical conductivity σ ($m = 0$), (g) Seebeck coefficient S ($m = 1$), and (h) the Lorenz number ($m = 2$), which is related to the electronic thermal conductivity. The area under the curves are proportional to the magnitude of each transport coefficient at a fixed Fermi energy E_{F}.

isotropic conduction and valence bands with different effective masses and scattering times i.e., different weighted mobilities.

We can graphically understand the transport coefficients in a material with majority and minority carriers (Figure 1). In isotropic and parabolic bands, squared group velocity varies linearly with energy E as $v^2(E) \sim |E - E_b|$, where E_b is the band edge. The density of states of a parabolic band is given by $g(E) \sim \sqrt{|E - E_b|}$, and the scattering time due to polar optical phonons is expressed as $\tau(E) \sim \sqrt{|E - E_b|}$. By Eq. (1), the transport distribution function follows a squared energy dependence $\Sigma(E) \sim (E - E_b)^2$ as shown in Figure 1(d). The selection function $-\partial f/\partial E$, which peaks at the Fermi energy E_{F} (Figure 1e), samples $\Sigma(E)$ in both the conduction and valence bands, resulting in contributions from both bands to the transport coefficients σ (Figure 1f), S (Figure 1g), and κ_e (Figure 1h). The qualitative trends in the transport coefficients are not dependent on the scattering mechanism; similar results are obtained for acoustic deformation potential scattering (Figure S1).

Since the transport coefficients depend on the position of E_{F} relative to the valence and conduction band edges, it is convenient to define a reduced Fermi energy for each band separately. If we reference E_{F} to the majority carrier band edge i.e., $E_{\mathrm{F}} = 0$, then the reduced Fermi energy of majority carriers (η_{maj}) and minority carriers (η_{min}) are given by,

$$\begin{aligned} \eta_{maj} &= \frac{E_{\mathrm{F}}}{k_B T} \\ \eta_{min} &= -\eta_{maj} - \frac{E_g}{k_B T} \end{aligned} \tag{7}$$

where E_g is the band gap. For n-type (p-type), a positive E_{F} implies the Fermi energy lies inside the conduction (valence) band. It is important to note that the range of η_{maj} is bounded such that the majority carrier concentration is larger than minority carriers.

In a two-band model, $\Sigma(E)$ is the sum of the individual $\Sigma(E)$ of the valence (VB) and conduction (CB) bands. As a result, the electrical conductivity σ in a two-band model is

$$\sigma = \sigma_{maj} + \sigma_{min} \tag{8}$$

where σ_{maj} and σ_{min} are the single-band conductivities of majority and minority carriers, respectively, as defined in Eq. (4).

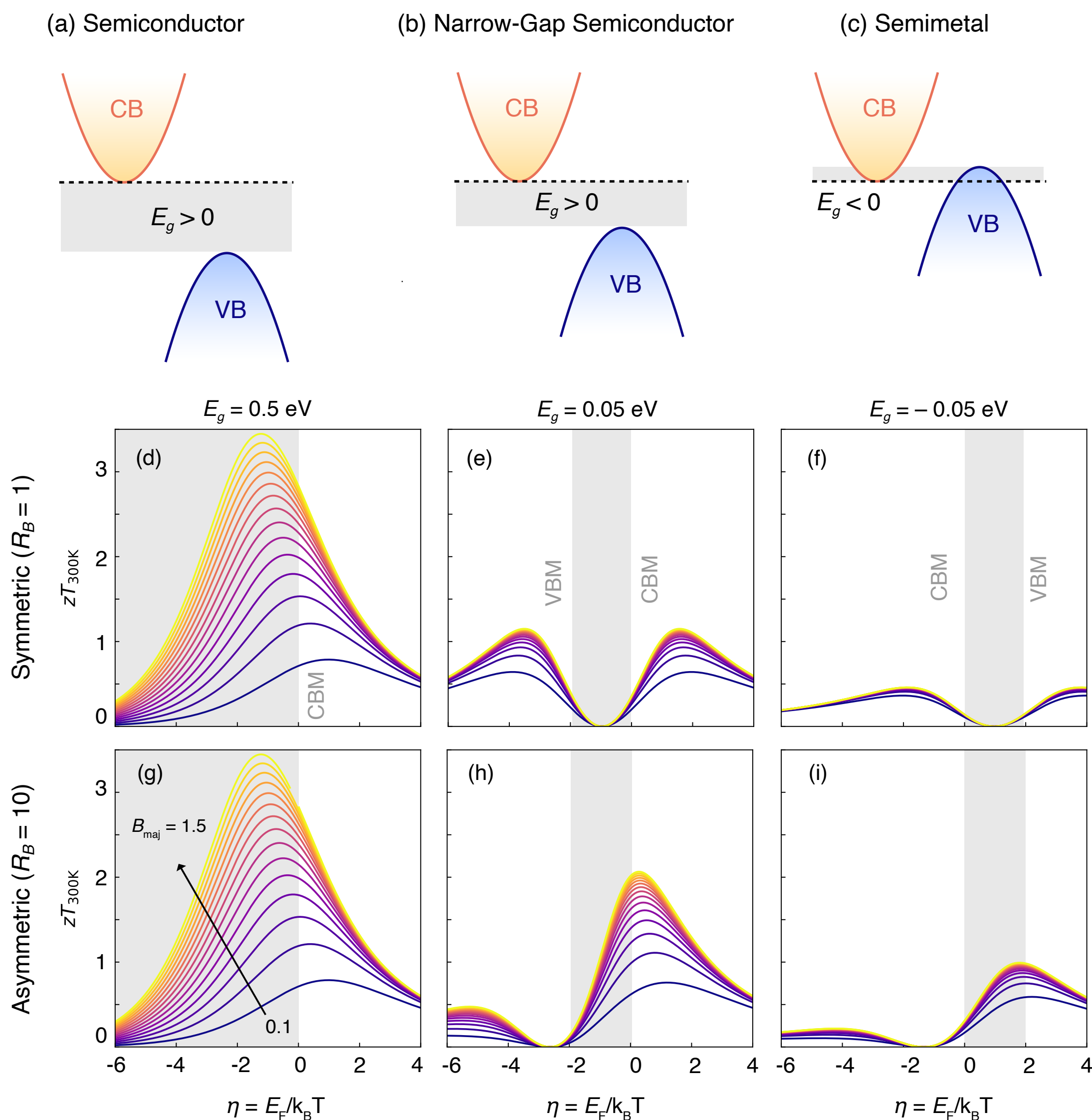

Fig. 2 zT as a function of the reduced Fermi energy (η) at 300 K for (a) semiconductors, (b) narrow-gap semiconductors, and (c) semimetals. The zT vs. η curves are plotted at 300 K for different B_{maj}, as defined in Eq. 14, assuming majority carriers are electrons. B_{maj} values range from 0.1 (dark blue) to 1.5 (yellow) in 0.1 increments. Panels (d) – (f) for the symmetric (R_B = 1) case. and panels (g) – (i) illustrate the case of large asymmetry (R_B = 10). For materials with narrow or negative band gap, large R_B is favorable for TE performance due to minimization of bipolar conduction effects.

The Seebeck coefficient S is given by,

$$S = \frac{S_{min} + S_{maj}\frac{\sigma_{maj}}{\sigma_{min}}}{1 + \frac{\sigma_{maj}}{\sigma_{min}}} \tag{9}$$

where S_{maj} and S_{min} are the single-band Seebeck coefficients of majority and minority carriers, respectively. Note that, by convention, the Seebeck coefficient of holes is positive and that of electrons is negative. The Lorenz number is

$$L = \frac{\left[L_{min} + S_{min}^2\right] + \left[L_{maj} + S_{maj}^2\right]\frac{\sigma_{maj}}{\sigma_{min}}}{1 + \frac{\sigma_{maj}}{\sigma_{min}}} - S^2 \tag{10}$$

where L_{maj} and L_{min} are the single-band Lorenz numbers of majority and minority carriers, respectively. The electronic thermal conductivity $\kappa_e = L\sigma T$ is,

$$\kappa_e = \kappa_{e,maj} + \kappa_{e,min} + \underbrace{\sigma T\left(\frac{S_{maj}^2}{1 + \frac{\sigma_{min}}{\sigma_{maj}}} + \frac{S_{min}^2}{1 + \frac{\sigma_{maj}}{\sigma_{min}}} - S^2\right)}_{\kappa_b} \tag{11}$$

where $\kappa_{e,maj}$ and $\kappa_{e,min}$ are the majority and minority carrier contributions to the thermal conductivity, respectively. The last summand in Eq. (11), κ_b, is often referred to as the “bipolar thermal conductivity”, which arises due to the presence of both electrons and holes.[59,60] Using the two-band transport coefficients

 This journal is © The Royal Society of Chemistry [year]

in Eq. (8) – (11), zT is expressed as,

$$zT = \frac{S^2\sigma T}{\kappa_e + \kappa_L} = \frac{S^2}{L + \frac{\kappa_L}{\sigma T}} \quad (12)$$

The term $\kappa_L/(\sigma T)$ can be expressed in terms of the majority and minority carrier quality factors, denoted B_{maj} and B_{min} respectively:

$$\frac{\kappa_L}{\sigma T} = \frac{(k_B/e)^2}{r+\frac{3}{2}} \frac{1}{F_{r+\frac{1}{2}}(\eta_{maj})B_{maj} + F_{r+\frac{1}{2}}(\eta_{min})B_{min}} \quad (13)$$

Here, the quality factors B_i are dimensionless

$$B_i = \left(\frac{k_B}{e}\right)^2 \frac{8\pi e}{3} \left(\frac{2m_e k_B}{h^2}\right)^{3/2} \frac{\mu_{w,i}T^{5/2}}{\kappa_L}, \quad i = maj, min \quad (14)$$

where B_{maj} and B_{min} are the B values of majority and minority carriers, respectively.

Charge transport is regulated by the conductivity ratio $\sigma_{maj}/\sigma_{min}$, as it appears in S (Eq. 9) and κ_e (Eq. 11). From the single-band model (Eq. 4), the conductivity ratio is

$$\frac{\sigma_{maj}}{\sigma_{min}} = R_B \frac{F_{r+\frac{1}{2}}(\eta_{maj})}{F_{r+\frac{1}{2}}(\eta_{min})} \quad (15)$$

where we define a material-dependent *asymmetry* parameter R_B,

$$R_B = \frac{\mu_{w,maj}}{\mu_{w,min}} = \frac{B_{maj}}{B_{min}} \quad (16)$$

which represents the relative contributions of majority and minority carriers to the overall charge transport. Note that "asymmetry" does not imply anisotropy i.e., direction dependence of transport properties. As a result, bipolar conduction effects in systems with both majority and minority carriers, such as narrow-gap semiconductors and semimetals, are significantly affected by R_B.

We compare zT for three representative cases of E_g: a semiconductor with a wide band gap (Figure 2a), a narrow-gap semiconductor (Figure 2b), and a semimetal (Figure 2c). Regardless of E_g, higher B_{maj} corresponds to higher zT for a given doping level η and temperature, as expected from a single-band model with no minority carriers.[35,61] As the band gap decreases (0.5 eV $\rightarrow$ 0.05 eV $\rightarrow$ -0.05 eV), the maximum zT decreases due to the detrimental effects of bipolar conduction. This behavior can be understood from the individual transport coefficients in Figure 3. σ is higher when the band gap is small or negative due to additive contributions from both electrons and holes (Figure 3b). However, S decreases due to the partial cancellation of opposite charge carrier contributions (Figure 3c), and the higher σ leads to a higher κ_e (Figure 3d).

Bipolar conduction effects in narrow-gap semiconductors and semimetals can be partially minimized when B_{min} is lower than B_{maj} i.e., $R_B > 1$. We show this by contrasting zT when the quality factors are nearly the same (Figures 2d – 2f) vs. asymmetric (Figures 2g – 2i). zT is nearly unaffected by R_B when the band gap is sufficiently large (Figures 2d and 2g). However, the benefit of a higher R_B is more noticeable when the band gap is smaller; in particular, zT is higher for a given doping level and temperature when R_B is higher (Figures 2e – 2f, 2h – 2i). For a given B_{maj}, a higher $R_B = B_{maj}/B_{min}$ corresponds to a lower B_{min}, meaning that we minimize minority carrier contributions to the overall TE transport. σ of minority carriers therefore decreases for higher R_B, leading to a decrease in the overall σ (Figure 3b). However, κ_e is correspondingly lower (Figure 3d) and, more notably, the magnitude of the Seebeck coefficient is higher because the cancellation of opposite charge carriers is minimized (Figure 3c). In effect, higher asymmetry between the quality factor of majority and minority carriers mitigates the detrimental effects of bipolar conduction in narrow-gap semiconductors and semimetals. We arrive at the same qualitative conclusions regardless of the scattering mechanism, as evident from comparing Figure 2 and Figure S2, and Figure 3 and Figure S3.

It is worth noting cases where transport by majority and minority carriers are asymmetric but in favor of minority carriers, i.e., $R_B < 1$. For a given E_g, zT is lower when $R_B < 1$ as illustrated in Figures 3e – 3f. Since the transport properties of minority carriers in this case are favorable over those of majority carriers, zT is maximized only when the material is nearly intrinsic and the concentrations of opposite carrier types are roughly the same (Figure S4). The implication of $R_B < 1$ is that the material will display better TE performance by switching the majority carrier type. For example, if $R_B < 1$ and electrons are assumed to be the majority carriers, the material will be better as a p-type material instead when holes are the majority carrier type. This is consistent with the overall framework. In summary,

1. Semiconductors with large E_g will not suffer from bipolar conduction effects and exhibit higher maximum zT.

2. Large B_{maj} indicates high TE performance *in the absence of bipolar conduction*.

3. zT of narrow-gap semiconductors and semimetals is sensitive to the asymmetry parameter i.e., $R_B = B_{maj}/B_{min}$. When the asymmetry is in favor of the majority carriers i.e., $R_B > 1$, the material exhibits higher zT because bipolar conduction effects are minimized.

Therefore, we use E_g, B_{maj}, and R_B as material descriptors to search for room-temperature TE materials that are narrow-gap semiconductors or semimetals. Prior studies have identified the importance of transport asymmetry to minimize bipolar conduction and achieve high power factors in narrow gap materials.[62–64] Our analysis is in agreement with these prior studies. However, these studies relied on either full-zone electrical transport calculations or a large number of descriptors obtained through parameter combinations. In contrast, we derive the functional dependence of TE performance on R_B from the two-band model. Also, prior work has focused on narrow-gap materials. Our proposed descriptors are applicable to both narrow-gap semiconductors *and* semimetals, which is important to account for well-known low-temperature TE materials such as Mg_3Bi_2.

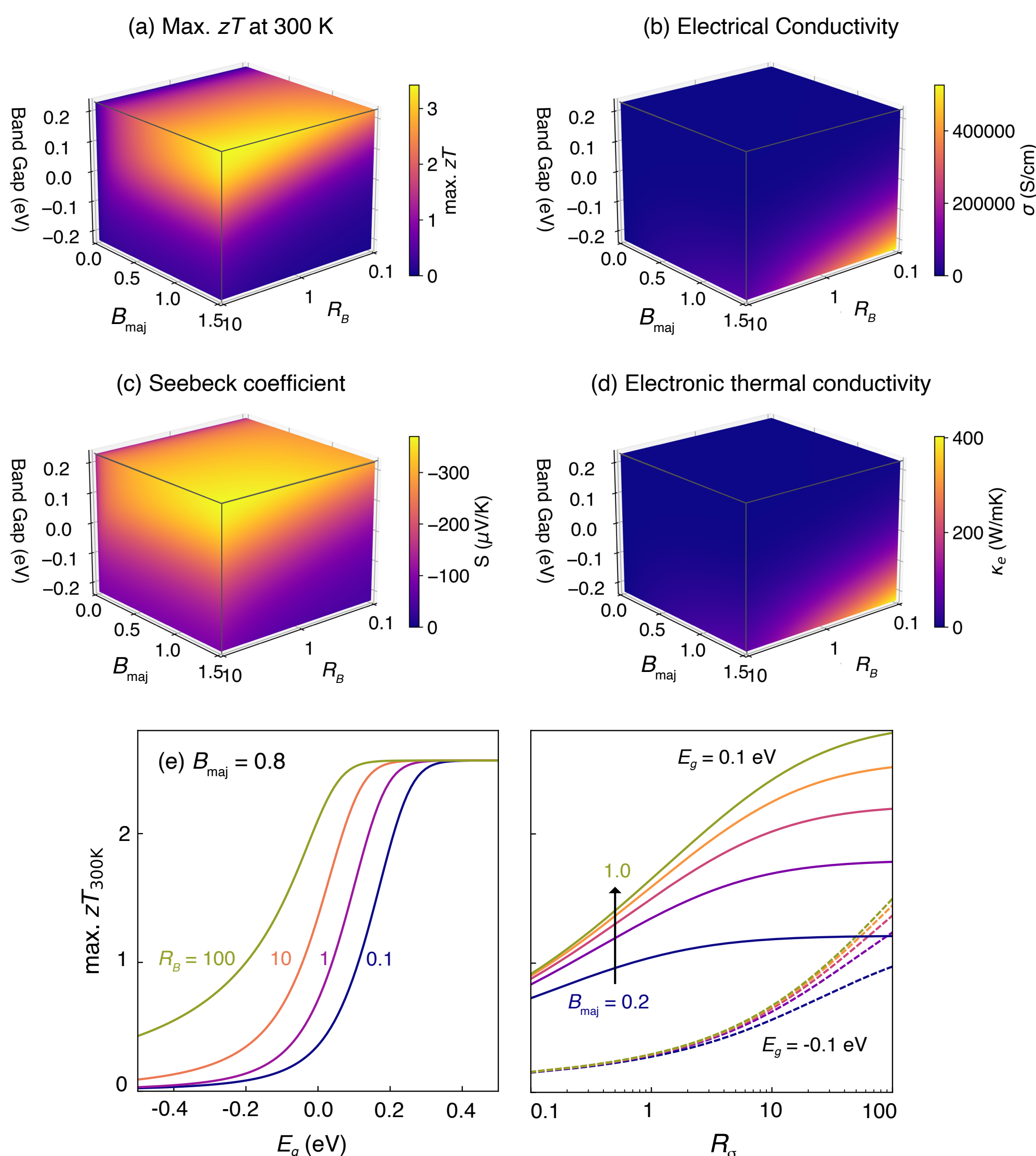

Fig. 3 (a) Maximum zT at 300 K as a function of band gap (E_g), majority carrier quality factor (B_{maj}), and asymmetry parameter (R_B). The electrical conductivity (b), Seebeck coefficient (c), and electronic thermal conductivity (d) are shown at the E_F where zT is maximized at 300 K. (e) Maximum zT at 300 K as a function of band gap, assuming $B_{maj} = 0.8$. Each curve corresponds to different R_B. (f) Maximum zT at 300 K for different R_B, shown for E_g = 0.1 eV (solid) and E_g = -0.1 eV (dashed). Each curve corresponds to different B_{maj}. Wide-gap materials exhibit high zT; however, high TE performance is also achieved in narrow-gap semiconductors and semimetals with high B_{maj} and R_B.

3 Application: Search for Narrow-Gap and Semimetallic Thermoelectric Materials

3.1 Computational Workflow

We apply the proposed material descriptors to computationally search for room-temperature TE materials among narrow-gap and semimetallic Zintl phases. The search focuses on Zintl phases because they are known to have narrow and negative band gaps, and generally exhibit good TE performance.[65] The tiered computational workflow is depicted in Figure 4. Details of the density functional theory (DFT) and other calculations, as well as the workflow, are provided in Section 6.

Out of 650 Zintl phases from the Inorganic Crystal Structure Database (ICSD), we identify 44 phases that are potentially narrow-gap semiconductors or semimetals using DFT with the semilocal PBE functional. By calculating the maximum zT at 300 K (Section 2), we identify 28 promising Zintl phases, for which we perform more accurate electronic structure calculations with hybrid DFT functional. The computed material descriptors for these 28 phases, in addition to the benchmark materials Mg_3Bi_2, Bi_2Te_3, and Bi_2Se_3, are reported in Table S1. The predicted zT_{max} at 300 K as a function of the transport asymmetry (R_B) and band gap (E_g) are plotted in Figure 5a. Below, we discuss the material descriptors and predicted TE performance of Mg_3Bi_2, Bi_2Te_3, and the three best candidate Zintl phases.

 This journal is © The Royal Society of Chemistry [year]

Table 1 Material properties and descriptors of Mg_3Bi_2, Bi_2Te_3, and three candidate Zintl phases calculated with the hybrid HSE06 functional, including spin-orbit coupling. E_g is the band gap in eV, $N_{V,VB}$ and $N_{V,CB}$ are the valence and conduction band valley degeneracies, respectively, B_p and B_n are the TE quality factors of p- and n-type, respectively, and R_B is the asymmetry parameter. The maximum zT is calculated at 300 K assuming polar optical scattering ($r = 1/2$).

Compound	E_g	$N_{V,VB}$	B_p	$N_{V,CB}$	B_n	R_B	max. $zT_{300\text{K}}$	n-/p-type
Mg_3Bi_2	-0.11	1	0.002	6	0.021	11.0	0.32	n
Bi_2Te_3	0.18	6	0.011	2	0.006	1.7	0.26	p
Bi_2Se_3	0.32	1	0.003	1	0.004	1.4	0.11	n
$SrSb_2$	0.32	3	0.011	4	0.018	1.6	0.39	n
Zn_3As_2	0.44	2	0.004	3	0.012	2.9	0.29	n
NaCdSb	0.41	2	0.006	2	0.009	1.5	0.23	n

3.2 Validation and Materials Recommendations

Mg_3Bi_2: Recent work on Mg_3Bi_2-based materials have demonstrated their excellent room-temperature TE performance, which rivals the state-of-the-art Bi_2Te_3-based materials.[66] The superior TE performance of Mg_3Bi_2 is despite the fact that it is a semimetal with a measured band gap of -0.1 eV.[14] Recall from the analysis in Section 2 that semimetals are generally at a disadvantage due to increased bipolar conduction. Our calculated band gap (with HSE06+SOC) of -0.11 eV is in good agreement the experimentally measured value. The computed TE quality factors (Table 1) yield an $R_B = 11$, which is the highest among the structures calculated with the hybrid DFT functional. The large B_n and R_B is mainly a result of the high conduction band degeneracy $N_{V,CB}$ of 6 (Figure 5b). Based on the descriptors, we find that Mg_3Bi_2 is one of the best-performing room-temperature TE material (high n-type $zT_{300\text{K}}$) among the narrow-gap and semimetallic Zintl phases considered in this study (Figure 5a). In fact, the predicted zT_{max} of 0.32 at 300 K (Table 1) is close to the experimental value when doped with Te ($zT \sim 0.3$). The "rediscovery" of Mg_3Bi_2 provides validation for our computational search workflow. Note that high TE performance at room temperature is achieved by alloying Mg_3Bi_2 with Mg_3Sb_2.[14] Mg_3Sb_2 also has a large conduction band degeneracy of 6,[67] which yields a large R_B of 7.6, and $zT_{300K} = 0.28$ for n-type (Table S1).

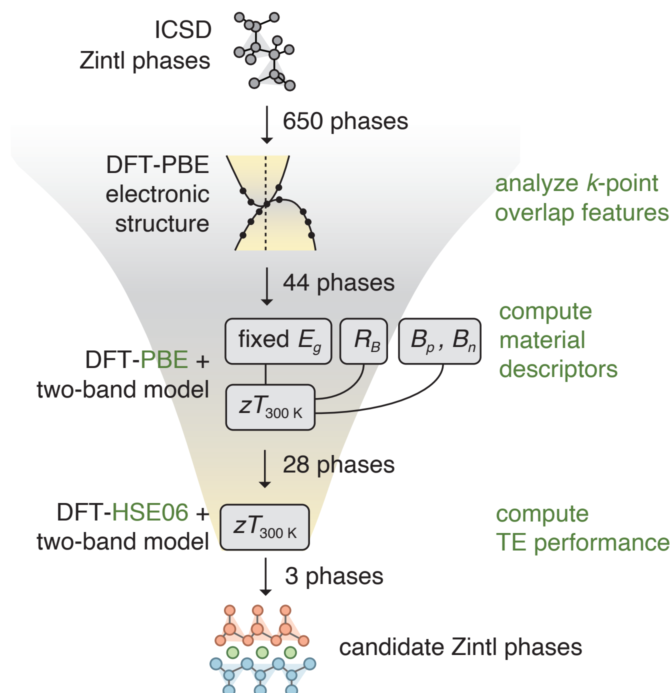

Fig. 4 Computational workflow to identify Zintl phases that are narrow-gap semiconductors or semimetals and exhibit high room-temperature thermoelectric performance. E_g is the band gap, R_B is the asymmetry parameter, and B_{maj} and B_{min} are the quality factors of majority and minority carriers. PBE and HSE06 refer to DFT functionals (see Methods).

Bi_2Te_3: Bi_2Te_3-based materials have been the state-of-the-art low-temperature TE materials for commercial devices.[13] Bi_2Te_3 has a small band gap of 0.14 eV,[13] which is in agreement with our calculated value of 0.18 eV from HSE+SOC (see Table 1). Bipolar conduction effects are expected to be non-negligible in such small band gap materials. We identify Bi_2Te_3 as a high-performing TE material with a maximum p-type zT of 0.26 at 300 K, assuming polar optical scattering.[68] The high TE performance can be partly attributed to the intrinsically high valley degeneracy and low carrier effective mass.[13] In contrast, the TE performance of Bi_2Se_3 is predicted to be lower with a maximum zT of 0.11 at 300 K since the valley degeneracies and, correspondingly, the TE quality factors, are low (Table 1). The identification of Bi_2Te_3 as a candidate material further validates the proposed descriptors and our computational workflow.

$SrSb_2$: This phase is predicted to have the highest zT at 300 K. $SrSb_2$ crystallizes in a monoclinic structure (space group $P2_1/m$, no. 11) composed of infinite 1-D Sb chains interspersed with Sr (Figure 5d).[69] $SrSb_2$ has a narrow band gap of 0.32 eV and valence and conduction band valley degeneracies of 3 and 4, respectively (Table 1). The Fermi surfaces are shown in 5d. An asymmetry parameter R_B of 1.6 results in a maximum n-type $zT_{300\text{K}}$ of 0.39, which is 1.22× larger compared to Mg_3Bi_2 and

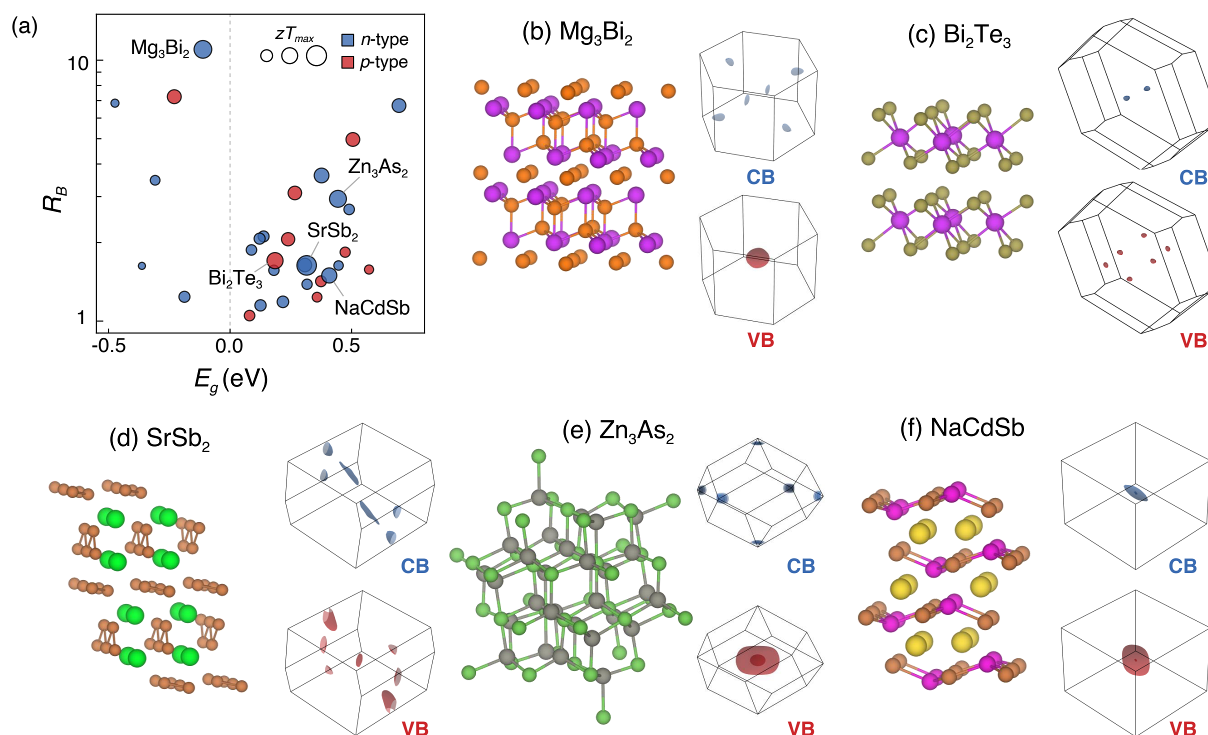

Fig. 5 (a) Predicted thermoelectric performance of 31 Zintl phases plotted as a function of the transport asymmetry (R_B) and the band gap (E_g). The marker size scales with the maximum zT at 300 K using the two-band model. The maximum zT are reported in Table 1. The crystal structures and Fermi surfaces of the conduction band (blue, labeled "CB") and valence band (red, labeled "VB") are shown for (b) Mg_3Bi_2, (c) Bi_2Te_3, and three candidate materials: (d) $SrSb_2$, (e) Zn_3As_2, (f) and NaCdSb.

1.5× compared to Bi_2Te_3. $SrSb_2$ has been used as a precursor for synthesizing Sr-filled $CoSb_3$ through arc-melting,[70,71] and small grains of $SrSb_2$ have been observed in the samples.[70] However, detailed characterization of transport properties has so far not been reported. Our predictions make $SrSb_2$ an interesting candidate to pursue experimentally.

Zn_3As_2. This semiconductor (E_g = 0.44 eV) adopts the Mn_2O_3-type structure (space group $Ia\bar{3}$, no. 206) and is one of several polymorphs of Zn_3As_2.[72] Several other polymorphs of Zn_3As_2 are known, including the room-temperature α phase ($I4_1/acd$),[73] the high-temperature α' phase ($P4_2/nbc$),[74,75] another high-temperature β phase ($Fm\bar{3}m$),[76] and the high-temperature, high-pressure α'' phase ($P4_2/nmc$).[77,78] The TE properties of Cd_3As_2-Zn_3As_2 alloys have been studied,[79–82] but the transport properties of the $Ia\bar{3}$ phase has not been measured. There are three conduction bands that are close in energy and located at the Brillouin zone edges (Figure 5e), yielding a valley degeneracy $N_{V,CB}$ of 3. There are two valence bands close in energy at the Γ-point, yielding a valley degeneracy $N_{V,VB}$ of 2. Despite a modest R_B of 2.9, the relatively large band gap of 0.44 eV facilitates a high TE performance. The lower performance compared to $SrSb_2$ is primarily due to the smaller B_n.

NaCdSb: This Zintl phase belongs to a large family of ternary ABX Zintl phases that adopt many different structure types.[43] NaCdSb crystallizes in an orthorhombic structure ($Pnma$, no. 62) with distorted square pyramidal $NaSb_5$ units, which share edges with $CdSb_4$ tetrahedra.[83,84] The structure can also be visualized as corrugated $(CdSb)^{1-}$ layers arranged in a honeycomb structure and intercalated with Na (Figure 5f). The material is predicted to be semiconducting with a band gap of 0.41 eV. The individual TE quality factors yield an R_B of 1.5. Overall, we predict the maximum zT_{300K} of NaCdSb to be 72% of the maximum zT_{300K} of Mg_3Bi_2. Guo et al. recently reported experimentally measured zT_{300K} of 0.2 without optimizing of carrier concentration.[85] The highest zT of the material was found to be 1.3 at 673 K.

4 Thermoelectric Quality Factor for Narrow-gap Semiconductors

We identified three material descriptors that are important to describe the TE performances of narrow-gap semiconductors and semimetals: majority carrier quality factor (B_{maj}), band gap (E_g), and the asymmetry parameter (R_B). We used these descriptors to efficiently search for new TE materials with narrow or negative band gaps for room-temperature TE applications. Our search methodology based on these descriptors is distinct from previous studies that assume absence of minority carrier effects.[29,32] In the case of single-band transport, the maximum zT of a material is solely determined by the quality factor (B) of the majority carriers and it monotonically increases with B (Figure S5). Prior studies have used B as a descriptor to search for high-performing TE materials.[32,86,87] However, a composite descriptor

 This journal is © The Royal Society of Chemistry [year]

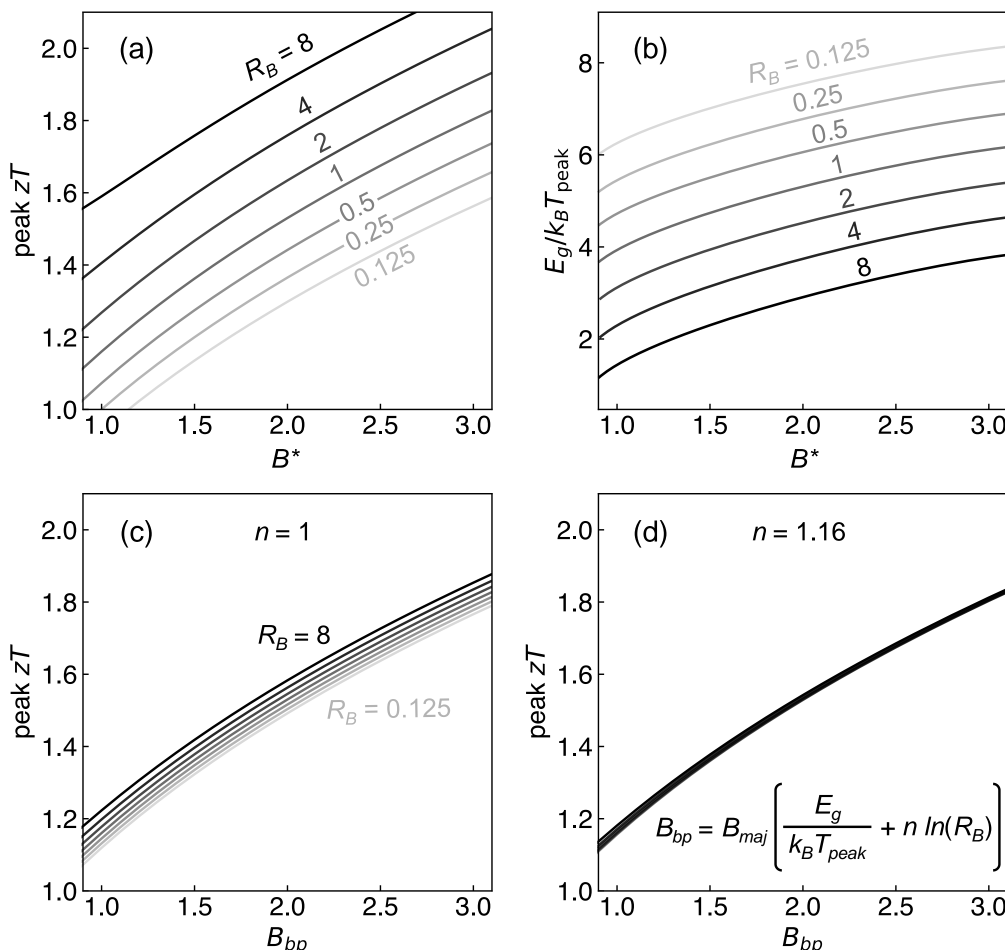

Fig. 6 (a) Peak zT and (b) E_g/k_BT_{peak} plotted against B^* (Eq. 17) for different values of R_B. Peak zT plotted against B_{bp} (Eq. 18) is shown for (c) n = 1 and (d) n = 1.16.

that provides a measure of peak zT i.e., optimized with respect to doping *and* temperature, for two-band transport is currently missing. To address this need, we propose a refined TE quality factor, B_{bp}, where "bp" denotes "bipolar".

B_{bp} is a useful descriptor of TE performance when both majority and minority carriers significantly contribute to charge transport, for example, in narrow-gap semiconductors. The mathematical form of B_{bp} should ideally have the following characteristics: (*i*) increase monotonically with peak zT, (*ii*) include B_{maj}, E_g, and R_B, and (*iii*) be interpretable to understand the relative contribution of each parameter to peak zT. Liu et al. defined a parameter B^*, which describes the relative contributions of two of the three descriptors, B_{maj} and E_g, towards the peak zT:[88–90]

$$B^* = B_{maj}\frac{E_g}{k_BT_{peak}} \tag{17}$$

where T_{peak} is the temperature corresponding to peak zT. Note that T_{peak} is a material property that depends on B_{maj}, E_g, and R_B. The peak zT at a given R_B value monotonically increases with B^* (Figure 6a). The E_g/k_BT_{peak} curve as a function of B^* shows a nearly-constant shift when R_B changes by some multiplicative factor (Figure 6b), suggesting an additive correction to E_g/k_BT_{peak} that depends logarithmically on R_B. We therefore propose the following mathematical form of B_{bp}:

$$B_{bp} = B_{maj}\left[\frac{E_g}{k_BT_{peak}} + n\ln(R_B)\right] \tag{18}$$

where n is a fitted parameter. As shown in Figure 6c, with n = 1, peak zT still varies noticeably with the choice of R_B. We find that $n = 1.16$ yields a satisfactory fit with only 3% spread in peak zT when R_B is changed by a factor of 64 (Figure 6d). We also find that the functional dependence in Eq. 18 is valid for various scattering mechanisms, which are implemented through our choice of the scattering parameter r (Figure S6).

We calculate B_{bp} and the corresponding peak zT for the narrow-gap Zintl phases (Figure S7). We find that candidate materials identified in our search ($SrSb_2$, Zn_3As_2, and NaCdSb) have fairly high B_{bp} values, as well as other Zintl phases such

This journal is © The Royal Society of Chemistry [year]

as Mg_2ZnAs_2, $NaZn_4As_3$, and $Li_4Ba_3As_4$. We note that ranking the TE performances of narrow-gap semiconductors with B_{bp} is fundamentally different from the search methodology employed in Section 3. B_{bp} is a measure of the peak performance at the corresponding T_{peak} and optimized doping level. T_{peak} need not be 300 K, which was the focus of the search presented in Section 3. On the other hand, using B_{maj}, E_g, and R_B as separate descriptors allows us to compare the TE performances of materials at assumed temperatures or doping levels, or both. In Section 3 for example, we rank the TE performance of Zintl phases at room temperature (300 K). Using the individual descriptors (B_{maj}, E_g, R_B) allow us to search for materials for specific low-temperature applications, for example, at or near room temperature for IoT sensors.[11,12]

5 Conclusions

We use an analytical two-band model to derive material descriptors for predicting the TE performances of narrow-gap semiconductors and semimetals. The proposed descriptors are obtained from simple DFT calculations, which allows reliable, high-throughput search of narrow-gap semiconductors and semimetals for low-temperature thermoelectrics. We find that the material descriptors that govern TE performance are: (1) the majority carrier quality factor (B_{maj}), (2) the band gap (E_g), and (3) the asymmetry in the transport properties of majority and minority carriers ($R_B = B_{maj}/B_{min}$), where B_{min} is the minority carrier quality factor. As in a single-band model, materials with high quality factors tend to exhibit high TE performance when doping is optimized. However, high TE performance in narrow-gap semiconductors and semimetals also hinges on minimizing bipolar conduction effects, which is achieved when majority and minority carrier transport is asymmetric, i.e., when R_B is large. Using the proposed material descriptors, we assess the TE performances of a set of narrow-gap and semimetallic Zintl phases. In agreement with experiments, we correctly re-identify Mg_3Bi_2 and Bi_2Te_3 as high-performing TE materials for room-temperature applications. In particular, Mg_3Bi_2 showcases the importance of transport asymmetry; despite being a semimetal, a large R_B ensures high room-temperature TE performance. From our search, we find three Zintl phases ($SrSb_2$, Zn_3As_2, and NaCdSb) that exhibit high room-temperature TE performance. We further propose a refined TE quality factor, B_{bp}, which is a useful measure of the TE performance when bipolar conduction effects are significant. B_{bp} combines the individual descriptors (B_{maj}, E_g, and R_B) into a single metric to assess the peak zT of materials.

While the descriptors help to identify candidate TE materials, there are others factors that require careful consideration for practical applications. The temperature-dependence of E_g for example may affect the predicted maximum zT at 300 K. The negative E_g of Mg_3Bi_2 changes by $\sim$25 meV within a range of 350 K,[14] and E_g of Bi_2Te_3 changes by $\sim$100 meV within a range of 600 K.[91] We find that for Bi_2Te_3 and the three candidate Zintl phases, maximum zT at 300 K does not change significantly if the band gap is changed by 25 meV or 100 meV (Table S2). Maximum zT of Mg_3Bi_2 however, owing to its negative band gap, is most sensitive to changes in E_g, as illustrated in Figure 3e. Oxidation is another consideration for terrestrial applications.[92] Near room-temperature operation will reduce the effects of oxidation due to sluggish kinetics, but experimental verification is needed especially for materials containing alkali and alkaline-earth elements. Materials also need to be doped to optimize TE performance. Generally, narrow band gap semiconductors are more easily dopable compared to wide-gap insulators due to low concentrations of charge compensating native defects.[93] Future work should address these key considerations in optimizing the TE performance of the candidate materials.

6 Computational Methodology

A schematic of the computational workflow is shown in Figure 4. We use first-principles density functional theory (DFT) to perform structural relaxations, and to calculate electronic band structures and bulk moduli. All DFT calculations are performed with the Vienna *Ab initio* Simulation Package (VASP)[94,95] and the projector augmented wave (PAW) method is used to describe the core electrons.[96,97] The wavefunctions are expanded as plane waves with an energy cutoff of 340 eV.

First, we relax the ICSD structures of 650 Zintl phases using the generalized gradient approximation (GGA) of Perdew-Burke-Ernzerhof (PBE)[98] as the exchange correlation functional and an automatically-generated Γ-centered k-point mesh with length factor $R_k = 20$. We apply on-site Hubbard U corrections on the d orbitals of certain transition metals, following the methodology in Refs. 41 and 99. For the relaxed structures, we computed their electronic structures on a dense Γ-centered k-mesh determined by the equation $N_{\rm atoms} \times N_{\rm kpts} \approx 8000$, where $N_{\rm atoms}$ and $N_{\rm kpts}$ are the number of atoms in the primitive cell and number of k-points, respectively.[43,44] This translates to a k-point grid of $14 \times 14 \times 8$ for Mg_3Bi_2 and $12 \times 12 \times 12$ for Bi_2Te_3. We include relativistic spin-orbit coupling (SOC) effects in these calculations.

Next, we analyze features of the electronic structures calculated with the PBE functional. It is well-known that semilocal DFT functionals such as GGA-PBE tend to severely underestimate the band gaps of materials, while predictions with hybrid functionals (e.g., HSE06) are generally more reliable for semiconductors and insulators.[100–102] However, the large computational cost associated with hybrid functionals makes them unsuitable for high-throughput calculations. Within the dataset of 650 Zintl phases, we focus on compounds that have zero or negative band gap in GGA-PBE calculations and try to identify potentially narrow-gap semiconductors and semimetals. We choose to focus on this subset of materials to demonstrate the usefulness of the descriptors in materials where bipolar conduction cannot be ignored. The specific procedure we have adopted to identify narrow-gap semiconductors and semimetals is not important because the descriptors are generally applicable irrespective of the band gap.

We analyze the band occupations to assess the extent of band overlap (nesting) near the Fermi level. In a typical semiconductor with a well-defined band gap, bands below the Fermi level are fully occupied (valence bands) and those above are unoccupied (conduction bands) at 0 K (DFT calculation). In this case, there are no partially occupied bands. In contrast, a metal is characterized by overlapping bands with partial occupancies at numerous

This journal is © The Royal Society of Chemistry [year]

k-points around the Fermi level. We therefore evaluate the fraction of partially-occupied k-points relative to the total number of sampled k-points. If this fraction is small, it is possible that the material is a narrow-gap semiconductor or semimetal, but less likely to be a true metal. Specifically, we calculate the ratio,

$$R = \frac{\sum_{n=n_1}^{n_2} \sum_k P\left(O_{n,k}\right)}{2N_{\text{kpts}}(N+1)}$$
$$n_1 = \frac{n_e}{2} - N, \;\; n_2 = \frac{n_e}{2} + N + 1 \tag{19}$$

where n is the band index, n_e is the number of electrons, and N is the number of bands considered below and above the band index $n_e/2$, which in the case of a semiconductor will correspond to the index of the valence band maximum. $O_{n,k}$ is the occupation of the band n at a specific k-point. Here, P is a Boolean function of $O_{n,k}$. For bands with indices n_1 through $n_e/2$, if $O_{n,k} < 2-\delta$ (assuming doubly occupied bands), $P = 1$ otherwise $P = 0$. Similarly, for band indices $n_e/2+1$ through n_2, $P = 1$ if $O_{n,k} > \delta$.

We use $N = 3$ and occupation tolerance $\delta = 10^{-3}$ to calculate R. R varies between 0 and 1, with $R = 0$ representing a semiconductor and large R indicating that the phase is likely a metal (Figure S8). We classified materials with $0 < R \leq 0.1$ from the GGA-PBE electronic structure as potential narrow-gap semiconductors and semimetals because of the small overlap between the nominal valence and conduction bands. Among the 650 Zintl phases, we identify 44 that have $R \leq 0.1$.

For these 44 Zintl phases, we then estimate the maximum zT at 300 K using the two-band transport model (Eq. 12). Three independent material descriptors are necessary to estimate zT: band gap (E_g), n- and p-type quality factors (B_n and B_p), and asymmetry parameter (R_B). Due to the unsystematic underestimation of the band gap in GGA-PBE calculations, we fix E_g to 0.3 eV for all 44 phases. Since larger E_g leads to higher zT (Figure 3), fixing E_g to 0.3 eV allows us to compare the best-case-scenario zT across materials. We perform a scissor operation to adjust E_g with the assumption that the band geometry remains unchanged. The band effective mass m_b^* is an important parameter in calculating the quality factors and, therefore, R_B. We use a finite-difference method to calculate m_b^* from the electronic structure calculated on a dense k-point grid.[103] We also calculate the density-of-states effective mass m^*_{DOS} from m_b^* using the relation $m^*_{\text{DOS}} = N_V^{2/3} m_b^*$, where N_V is the valley degeneracy. The quality factors are then calculated using Eq. 14, where μ_0 and κ_L at 300 K are calculated using semi-empirical models that are fitted to large experimental datasets (see Refs. 32 and 86 for details). The bulk modulus, which is an input parameter for the semi-empirical models, is calculated by fitting the the Birch-Murnaghan equation of state to a set of total energies at different volumes.[104] In each case, we adjust the Fermi energy to maximize zT at 300 K.

Due to the recent success of Mg_3Bi_2-based materials for low- and room-temperature TE applications,[14] we compare the estimated maximum zT of the 44 Zintl phases to that of Mg_3Bi_2. We find that 20 out of the 44 Zintl phases have an estimated maximum zT of more than 20% of the maximum zT of Mg_3Bi_2 at 300 K. We perform higher accuracy electronic structure calculations with the hybrid HSE06 functional on the 20 phases, in addition to 8 randomly-chosen Zintl phases out of the remaining 24 phases. The exchange mixing parameter is set to 25%, and all HSE06 calculations include spin-orbit coupling effects. The structures are relaxed with HSE06 prior to calculating the electronic structure. We use the HSE06 electronic structure to calculate E_g and m_b^*, which are then used as inputs to estimate the maximum zT at 300 K. The corresponding results are shown in Figure 5a and tabulated in Tables 1 and S1.

CRediT Statement

Michael Y. Toriyama: Conceptualization, Investigation, Data Curation, Writing (Original Draft), Writing (Editing). **Adam N. Carranco**: Investigation, Data Curation, Writing (Editing). **G. Jeffrey Snyder**: Investigation, Writing (Editing), Supervision. **Prashun Gorai**: Conceptualization, Investigation, Data Curation, Writing (Editing), Supervision, Project Administration.

Acknowledgements

M.Y.T. is funded by the United States Department of Energy through the Computational Science Graduate Fellowship (DOE CSGF) under grant number DE-SC0020347. A.N.C. was funded by the Mines Undergraduate Research Fellowship (Colorado School of Mines). G.J.S. acknowledges award 70NANB19H005 from U.S. Department of Commerce, National Institute of Standards and Technology as part of the Center for Hierarchical Materials Design (CHiMaD). P.G. acknowledges support from NSF through award DMR-2102409. The research was performed using computational resources sponsored by the Department of Energy's Office of Energy Efficiency and Renewable Energy and located at the NREL.

Conflicts of Interest

There are no conflicts to declare.

References

1 Y. Dong, M. Coleman and S. A. Miller, *Annu. Rev. Env. Resour.*, 2021, **46**, 59.
2 J. M. Calm, *Int. J. Refrig.*, 2006, **29**, 833.
3 B. Xiang, P. K. Patra, S. A. Montzka, S. M. Miller, J. W. Elkins, F. L. Moore, E. L. Atlas, B. R. Miller, R. F. Weiss, R. G. Prinn and S. C. Wofsy, *P. Natl. A. Sci.*, 2014, **111**, 17379.
4 P. Purohit and L. Höglund-Isaksson, *Atmos. Chem. Phys.*, 2017, **17**, 2795.
5 *The Future of Cooling*, https://www.iea.org/reports/the-future-of-cooling.
6 X. Zhou, D. Yan, J. An, T. Hong, X. Shi and X. Jin, *Energ. Buildings*, 2018, **169**, 344.
7 G. J. Snyder, S. LeBlanc, D. Crane, H. Pangborn, C. E. Forest, A. Rattner, L. Borgsmiller and S. Priya, *Joule*, 2021, **5**, 748.
8 Q. Liu, F. Wei, G. Li, Z. Kan, J. Yang, H. Zhu, B. Wang and H. Zhao, *iScience*, 2022, **25**, 104296.
9 M. Abdullah, J. Ngui, K. Abd. Hamid, S. Leo and S. Tie, *Energ. Fuel*, 2009, **23**, 5677.

10 H. Moria, M. Ahmed, A. Alghanmi, T. I. Mohamad and Y. Yaakob, *Energy Procedia*, 2019, **158**, 198.
11 D. Narducci, *J. Phys. Energy*, 2019, **1**, 024001.
12 A. Grigoriev, S. Grigoriev, A. Korolev, O. Losev, D. Mel'nik, V. Skorlygin and A. Frolov, *Atom. Energy*, 2019, **125**, 231.
13 I. T. Witting, T. C. Chasapis, F. Ricci, M. Peters, N. A. Heinz, G. Hautier and G. J. Snyder, *Adv. Electron. Mater.*, 2019, **5**, 1800904.
14 J. Mao, H. Zhu, Z. Ding, Z. Liu, G. A. Gamage, G. Chen and Z. Ren, *Science*, 2019, **365**, 495.
15 Y. Liu, L. Yin, W. Zhang, J. Wang, S. Hou, Z. Wu, Z. Zhang, C. Chen, X. Li, H. Ji, Q. Zhang, Z. Liu and F. Cao, *Cell Rep. Phys. Sci.*, 2021, **2**, 100412.
16 Z. Liu, W. Gao, H. Oshima, K. Nagase, C.-H. Lee and T. Mori, *Nat. Commun.*, 2022, **13**, 1120.
17 J. Yang, G. Li, H. Zhu, N. Chen, T. Lu, J. Gao, L. Guo, J. Xiang, P. Sun, Y. Yao, R. Yang and H. Zhao, *Joule*, 2022, **6**, 193.
18 D.-Y. Chung, T. P. Hogan, M. Rocci-Lane, P. Brazis, J. R. Ireland, C. R. Kannewurf, M. Bastea, C. Uher and M. G. Kanatzidis, *J. Am. Chem. Soc.*, 2004, **126**, 6414.
19 R. Wolfe and G. Smith, *Appl. Phys. Lett.*, 1962, **1**, 5.
20 H. Wang, X. Luo, W. Chen, N. Wang, B. Lei, F. Meng, C. Shang, L. Ma, T. Wu, X. Dai, Z. Wang and X. Chen, *Sci. Bull.*, 2018, **63**, 411.
21 S. A. Miller, I. Witting, U. Aydemir, L. Peng, A. J. Rettie, P. Gorai, D. Y. Chung, M. G. Kanatzidis, M. Grayson, V. Stevanović, E. S. Toberer and G. J. Snyder, *Phys. Rev. Appl.*, 2018, **9**, 014025.
22 J. M. Tomczak, *Journal of Physics: Condensed Matter*, 2018, **30**, 183001.
23 P. Gorai, V. Stevanović and E. S. Toberer, *Nat. Rev. Mater.*, 2017, **2**, 1.
24 G. K. Madsen and D. J. Singh, *Comput. Phys. Commun.*, 2006, **175**, 67.
25 G. K. Madsen, J. Carrete and M. J. Verstraete, *Comput. Phys. Commun.*, 2018, **231**, 140.
26 A. Faghaninia, J. W. Ager III and C. S. Lo, *Phys. Rev. B*, 2015, **91**, 235123.
27 J.-J. Zhou, J. Park, I.-T. Lu, I. Maliyov, X. Tong and M. Bernardi, *Comput. Phys. Commun.*, 2021, **264**, 107970.
28 T. Deng, G. Wu, M. B. Sullivan, Z. M. Wong, K. Hippalgaonkar, J.-S. Wang and S.-W. Yang, *npj Comput. Mater.*, 2020, **6**, 1.
29 G. Xing, J. Sun, Y. Li, X. Fan, W. Zheng and D. J. Singh, *Phys. Rev. Mater.*, 2017, **1**, 065405.
30 R. Li, X. Li, L. Xi, J. Yang, D. J. Singh and W. Zhang, *ACS Appl. Mater. Inter.*, 2019, **11**, 24859.
31 Z. M. Gibbs, F. Ricci, G. Li, H. Zhu, K. Persson, G. Ceder, G. Hautier, A. Jain and G. J. Snyder, *npj Comput. Mater.*, 2017, **3**, 1.
32 J. Yan, P. Gorai, B. Ortiz, S. Miller, S. A. Barnett, T. Mason, V. Stevanović and E. S. Toberer, *Energ. Environ. Sci.*, 2015, **8**, 983.
33 P. Gorai, P. Parilla, E. S. Toberer and V. Stevanovic, *Chem. Mater.*, 2015, **27**, 6213.
34 A. F. May and G. J. Snyder, *Materials, preparation, and characterization in thermoelectrics*, CRC press, 2017, p. 207.
35 S. D. Kang and G. J. Snyder, *arXiv preprint arXiv:1710.06896*, 2017.
36 F. Ricci, A. Dunn, A. Jain, G.-M. Rignanese and G. Hautier, *J. Mater. Chem. A*, 2020, **8**, 17579.
37 T. Chasapis, D. Koumoulis, B. Leung, N. Calta, S.-H. Lo, V. Dravid, L.-S. Bouchard and M. Kanatzidis, *APL Mater.*, 2015, **3**, 083601.
38 H. Naithani, E. Müller and J. De Boor, *J. Phys. Energy*, 2022, **4**, 045002.
39 H. Wang, R. Gurunathan, C. Fu, R. Cui, T. Zhu and G. J. Snyder, *Mater. Adv.*, 2022, **3**, 734.
40 L. Zhang, P. Xiao, L. Shi, G. Henkelman, J. B. Goodenough and J. Zhou, *J. Appl. Phys.*, 2015, **117**, 155103.
41 P. Gorai, E. S. Toberer and V. Stevanović, *Phys. Chem. Chem. Phys.*, 2016, **18**, 31777.
42 S. A. Miller, P. Gorai, U. Aydemir, T. O. Mason, V. Stevanović, E. S. Toberer and G. J. Snyder, *J. Mater. Chem. C*, 2017, **5**, 8854.
43 P. Gorai, A. Ganose, A. Faghaninia, A. Jain and V. Stevanović, *Mater. Horiz.*, 2020, **7**, 1809.
44 J. Qu, V. Stevanović, E. Ertekin and P. Gorai, *J. Mater. Chem. A*, 2020, **8**, 25306.
45 N. W. Ashcroft and N. D. Mermin, *Solid State Physics*, Cengage Learning, 1976, vol. 3.
46 M. Lundstrom, *Fundamentals of carrier transport*, 2002.
47 B. M. Askerov, *Electron transport phenomena in semiconductors*, World scientific, 1994.
48 A. M. Ganose, J. Park, A. Faghaninia, R. Woods-Robinson, K. A. Persson and A. Jain, *Nat. Commun.*, 2021, **12**, 1.
49 Q. Song, T.-H. Liu, J. Zhou, Z. Ding and G. Chen, *Mater. Today Phys.*, 2017, **2**, 69.
50 J. Cao, J. D. Querales-Flores, A. R. Murphy, S. Fahy and I. Savić, *Phys. Rev. B*, 2018, **98**, 205202.
51 R. D'Souza, J. Cao, J. D. Querales-Flores, S. Fahy and I. Savić, *Phys. Rev. B*, 2020, **102**, 115204.
52 J. Ma, Y. Chen and W. Li, *Phys. Rev. B*, 2018, **97**, 205207.
53 G. J. Snyder, A. H. Snyder, M. Wood, R. Gurunathan, B. H. Snyder and C. Niu, *Adv. Mater.*, 2020, **32**, 2001537.
54 R. Simon, *J. Appl. Phys.*, 1962, **33**, 1830.
55 R. Simon, *Solid State Electron.*, 1964, **7**, 397.
56 G. Mahan, *J. Appl. Phys.*, 1989, **65**, 1578.
57 J. O. Sofo and G. Mahan, *Phys. Rev. B*, 1994, **49**, 4565.
58 Z. M. Gibbs, H.-S. Kim, H. Wang and G. J. Snyder, *Appl. Phys. Lett.*, 2015, **106**, 022112.
59 H.-S. Kim, K. H. Lee and S.-i. Kim, *J. Mater. Res. Tech.*, 2021, **14**, 639.
60 X. Shi, X. Zhang, A. Ganose, J. Park, C. Sun, Z. Chen, S. Lin, W. Li, A. Jain and Y. Pei, *Mater. Today Phys.*, 2021, **18**, 100362.

 This journal is © The Royal Society of Chemistry [year]

61 R. Chasmar and R. Stratton, *Int. J. Electron.*, 1959, **7**, 52.

62 P. Graziosi and N. Neophytou, *J. Phys. Chem. C*, 2020, **124**, 18462.

63 P. Graziosi, Z. Li and N. Neophytou, *Appl. Phys. Lett.*, 2022, **120**, 072102.

64 K. Ciesielski, I. Wolańska, K. Synoradzki, D. Szymański and D. Kaczorowski, *Phys. Rev. Appl.*, 2021, **15**, 044047.

65 S. M. Kauzlarich, S. R. Brown and G. J. Snyder, *Dalton T.*, 2007, 2099.

66 J. Mao, G. Chen and Z. Ren, *Nat. Mater.*, 2021, **20**, 454.

67 K. Imasato, M. Wood, S. Anand, J. J. Kuo and G. J. Snyder, *Adv. Energy Sustain. Res.*, 2022, **3**, 2100208.

68 B.-L. Huang and M. Kaviany, *Phys. Rev. B*, 2008, **77**, 125209.

69 K. Deller and B. Eisenmann, *Z. Naturforsch. B*, 1976, **31**, 1146.

70 G. Rogl, A. Grytsiv, N. Melnychenko-Koblyuk, E. Bauer, S. Laumann and P. Rogl, *J. Phys.-Condens. Mat.*, 2011, **23**, 275601.

71 G. Rogl and P. F. Rogl, *Front. Mater.*, 2020, **7**, 600261.

72 M. v. Stackelberg and R. Paulus, *Z. Phys. Chem. B*, 1933, **22**, 305.

73 G. De Vries, E. Frikkee, R. Helmholdt, K. Kopinga and W. De Jonge, *Physica B: Condensed Matter*, 1989, **156**, 321.

74 V. Lazarev, V. Guskov and J. Greenberg, *Mater. Res. Bull.*, 1981, **16**, 1113.

75 J. Greenberg, V. Guskov, V. Lazarev and A. Kotliar, *Mater. Res. Bull.*, 1982, **17**, 1329.

76 A. Pietraszko and K. Łukaszewicz, *Phys. Status Solidi A*, 1973, **18**, 723.

77 M. Stackelberg and R. Paulus, *Z. Phys. Chem.*, 1935, **28**, 427.

78 G. Chen, Z. Liu, B. Liang, G. Yu, Z. Xie, H. Huang, B. Liu, X. Wang, D. Chen, M.-Q. Zhu and G. Shen, *Adv. Funct. Mater.*, 2013, **23**, 2681.

79 L. Żdanowicz and W. Żdanowicz, *Phys. Status Solidi B*, 1964, **6**, 227.

80 G. Castellion and L. Beegle, *J. Phys. Chem. Solids*, 1965, **26**, 767.

81 D. P. Spitzer, G. A. Castellion and G. Haacke, *J. Appl. Phys.*, 1966, **37**, 3795.

82 V. Zakhvalinskii, T. Nikulicheva, A. Kochura, E. Lahderanta, M. Shakhov, A. Kubankin, M. Sukhov, M. Yaprintsev and A. Morocho, *AIP Adv.*, 2021, **11**, 035028.

83 G. Savelsberg, *Z. Naturforsch. B*, 1978, **33**, 370.

84 B. Courteau, V. Gvozdetskyi, S. Lee, T. Cox and J. V. Zaikina, *Z. Anorg. Allg. Chem.*, 2022, **648**, e202200095.

85 K. Guo, Y. Zhang, S. Yuan, Q. Tang, C. Lin, P. Luo, J. Yang, S. Pan, L.-D. Zhao, G. Cheng *et al.*, *Angew. Chem. Int. Edit.*, 2023, **62**, e202212515.

86 S. A. Miller, P. Gorai, B. R. Ortiz, A. Goyal, D. Gao, S. A. Barnett, T. O. Mason, G. J. Snyder, Q. Lv, V. Stevanović and E. S. Toberer, *Chem. Mater.*, 2017, **29**, 2494.

87 P. Graziosi, C. Kumarasinghe and N. Neophytou, *ACS Appl. Energ. Mater.*, 2020, **3**, 5913.

88 W. Liu, J. Zhou, Q. Jie, Y. Li, H. S. Kim, J. Bao, G. Chen and Z. Ren, *Energ. Environ. Sci.*, 2016, **9**, 530.

89 W. Liu, Z. Han, J. Ji, T. Feng, J. Yang and W. Zhang, *Mater. Today Phys.*, 2023, 100989.

90 X. Jia, S. Li, Z. Zhang, Y. Deng, X. Li, Y. Cao, Y. Yan, J. Mao, J. Yang, Q. Zhang and X. Liu, *Mater. Today Phys.*, 2021, **18**, 100371.

91 B. Monserrat and D. Vanderbilt, *Phys. Rev. Lett.*, 2016, **117**, 226801.

92 M. Y. Toriyama, D. Cheikh, S. K. Bux, G. J. Snyder and P. Gorai, *ACS Appl. Mater. Inter.*, 2022, **14**, 43517.

93 S.-H. Wei, *Comp. Mater. Sci.*, 2004, **30**, 337.

94 G. Kresse and J. Furthmüller, *Comp. Mater. Sci.*, 1996, **6**, 15.

95 G. Kresse and J. Furthmüller, *Phys. Rev. B*, 1996, **54**, 11169.

96 P. E. Blöchl, *Phys. Rev. B*, 1994, **50**, 17953.

97 G. Kresse and D. Joubert, *Phys. Rev. B*, 1999, **59**, 1758.

98 J. P. Perdew, K. Burke and M. Ernzerhof, *Phys. Rev. Lett.*, 1996, **77**, 3865.

99 V. Stevanović, S. Lany, X. Zhang and A. Zunger, *Phys. Rev. B*, 2012, **85**, 115104.

100 J. Heyd, G. E. Scuseria and M. Ernzerhof, *J. Chem. Phys.*, 2003, **118**, 8207.

101 J. Heyd and G. E. Scuseria, *J. Chem. Phys.*, 2004, **121**, 1187.

102 A. V. Krukau, O. A. Vydrov, A. F. Izmaylov and G. E. Scuseria, *J. Chem. Phys.*, 2006, **125**, 224106.

103 L. D. Whalley, J. M. Frost, B. J. Morgan and A. Walsh, *Phys. Rev. B*, 2019, **99**, 085207.

104 F. Birch, *J. Geophys. Res.*, 1952, **57**, 227.